Small-Animal PET/CT Imaging of Local and Systemic Immune Response Using ^{64}Cu-αCD11b

Qizhen Cao[1], Qian Huang[1], Chandra Mohan[2], and Chun Li[1]

[1]Department of Cancer Systems Imaging, The University of Texas M.D. Anderson Cancer Center, Houston, Texas; and [2]Department of Biomedical Engineering, University of Houston, Houston, Texas

Current noninvasive imaging methods for monitoring immune response were largely developed for interrogation of the local reaction. This study developed the radiotracer ^{64}Cu-labeled anti-CD11b (^{64}Cu-αCD11b) for longitudinal assessment of local and systemic immune response involving mobilization of CD11b^{+} myeloid cells by small-animal PET/CT. **Methods:** Acute or chronic inflammation in the ears of BALB/c mice was induced by 12-*o*-tetradecanoylphorbol-13-acetate. Acute lung inflammation was induced by intratracheal lipopolysaccharide inoculation. αCD11b was conjugated with *p*-SCN-Bn-DOTA followed by labeling with ^{64}Cu. PET/CT and biodistribution were evaluated at different times after intravenous injection of ^{64}Cu-αCD11b. Cell populations from bone marrow (BM) and spleen were analyzed by flow cytometry. **Results:** ^{64}Cu-αCD11b was primarily taken up by BM and spleen in control mice. In comparison, ^{64}Cu-αCD11b uptake was significantly reduced in the BM and spleen of CD11b-knockout mice, indicating that ^{64}Cu-αCD11b selectively homed to CD11b^{+} myeloid cells in vivo. In mice with ear inflammation, for the local inflammatory response, ^{64}Cu-αCD11b PET/CT revealed significantly higher ^{64}Cu-αCD11b uptake in the inflamed ears in the acute inflammation phase than the chronic phase, consistent with markedly increased infiltration of CD11b^{+} cells into the inflammatory lesions at the acute phase. Moreover, imaging of ^{64}Cu-αCD11b also showed the difference in mouse systemic response for different inflammatory stages. Compared with uptake in control mice, BM ^{64}Cu-αCD11b uptake in mice with ear inflammation was significantly lower in the acute phase and higher in the chronic phase, reflecting an initial mobilization of CD11b^{+} cells from the BM to the inflammatory foci followed by a compensatory regeneration of CD11b^{+} myeloid cells in the BM. Similarly, in mice with lung inflammation, ^{64}Cu-αCD11b PET/CT readily detected acute lung inflammation and recruitment of CD11b^{+} myeloid cells from the BM. Immunohistochemistry staining and flow cytometry results confirmed the noninvasive imaging of PET/CT. **Conclusion:** ^{64}Cu-αCD11b PET/CT successfully tracked ear and pulmonary inflammation in mice and differentiated acute from chronic inflammation at the local and systemic levels. ^{64}Cu-αCD11b PET/CT is a robust quantitative method for imaging of local and systemic immune responses.

Key Words: CD11b; PET/CT; inflammation; myeloid cells; systemic immune response

J Nucl Med 2019; 60:1317–1324
DOI: 10.2967/jnumed.118.220350

When local inflammation develops, myeloid cells expand in the bone marrow (BM), enter the blood circulation, and travel to the inflamed sites. Some myeloid cells transit through secondary lymphoid organs (i.e., the spleen). Local diseases can also elicit a systemic immune response secondary to release of cytokines and chemokines from the disease sites. Yet other diseases are marked by systemic inflammation to begin with, as in the case of systemic autoimmune diseases. Because different types of tissue injury at different stages of disease progression elicit different local and systemic inflammatory responses, the ability to longitudinally interrogate the depletion, migration, and expansion of immune cells throughout the whole body will greatly facilitate disease characterization and guide selection of appropriate treatment regimens.

Several imaging techniques have been used to monitor immune responses, including intravital optical imaging, MRI, and nuclear imaging, but all these techniques have limitations (*1,2*). Intravital optical imaging can directly visualize the dynamics of interactions among different types of cells; however, this technique suffers from limited penetration depth (*3*). MRI is useful for monitoring trafficking of infused immune cells labeled ex vivo but is not yet suitable for imaging biomarkers in specific immune cell populations labeled in vivo. In the area of nuclear imaging, several radiotracers have been reported to permit monitoring of inflammation on the basis of changes in metabolism (*4–6*) or ex vivo labeling of inflammatory cells or inflammatory cytokines (*7,8*), but it is limited by labeling efficiency and the labor-intensive cell labeling procedures (*9*). To date, few studies reported visualization of both the local and the systemic immune responses to inflammatory and neoplastic diseases (*10*).

Most innate inflammatory cells, including granulocytes, monocytes, and macrophages, express CD11b (also known as αM-integrin or Mac-1) on their cell surface (*11,12*). We hypothesized that CD11b could be used as an imageable biomarker for noninvasive assessment of local and systemic immune responses. In this work, we report the application of small-animal PET/CT with ^{64}Cu-labeled anti-CD11b (^{64}Cu-αCD11b) in monitoring the mobilization of CD11b^{+} myeloid cells from the BM to secondary lymphoid organs and to local inflammatory lesions.

MATERIALS AND METHODS

Reagents

Rat antimouse CD11b antibody (αCD11b, clone M1/70, catalog number 14-0112), rat antimouse CD11b phycoerythrin (clone M1/70), rat antimouse Gr-1 PerCP-cyanine5.5 (clone RB6-8C5), and rat antimouse Ly6C allophycocyanin (clone HK1.4) were purchased from eBioscience Inc. *p*-SCN-Bn-DOTA (*S*-2-(4-isothiocyanatobenzyl)-1,4,7,10-tetraazacyclododecane tetraacetic acid) was purchased from Macrocyclics, Inc. 12-*o*-tetradecanoylphorbol-13-acetate (TPA) was

---

Received Sep. 12, 2018; revision accepted Jan. 23, 2019.

For correspondence or reprints contact: Chun Li, Department of Cancer Systems Imaging, 1881 East Rd., Unit 1907, University of Texas M.D. Anderson Cancer Center, Houston, TX 77054.

E-mail: cli@mdanderson.org

purchased from Sigma-Aldrich. Lipopolysaccharide (*Escherichia coli* 0111) was purchased from List Biologics. ^{64}CuCl$_2$ and ^{18}F-FDG were obtained from the Cyclotron Radiochemistry Facility of the University of Texas M.D. Anderson Cancer Center.

DOTA Conjugation and Radiolabeling

p-SCN-Bn-DOTA was added to αCD11b or isotype-matched IgG at *p*-SCN-Bn-DOTA–to–antibody molar ratios of 50:1 in 0.1 M sodium bicarbonate buffer (pH 8.5). The resulting DOTA-αCD11b conjugate was purified using a PD-10 column, and the DOTA number for DOTA-αCD11b was measured (Supplemental Table 1; supplemental materials are available at http://jnm.snmjournals.org). For radiolabeling, ^{64}CuCl$_2$ was diluted with sodium acetate buffer (pH 6.0), and the pH of the solution was adjusted to 6.0 with 1N NaOH. Each DOTA-antibody conjugate was then added into ^{64}CuCl$_2$ solution (10 μg of DOTA-antibody per 37 MBq of ^{64}Cu) and incubated for 1 h at 38°C with constant shaking. ^{64}Cu-αCD11b or ^{64}Cu-IgG was purified by passage through a PD-10 column.

Number of DOTA per αCD11b Antibody

The average number of DOTA chelators per αCD11b antibody was measured according to reported procedures (*13–15*). Briefly, nonradioactive CuCl$_2$ (80-fold excess of DOTA-αCD11b) in 20 μL of 0.1N sodium acetate buffer (pH 5.5) was added to approximately 37 MBq of ^{64}CuCl$_2$ in 50 μL of 0.1N sodium acetate buffer; then, 20 μg of DOTA-αCD11b in 40 μL of 0.1N sodium acetate buffer were added to the above carrier-added ^{64}CuCl$_2$ solution. The reaction mixture was incubated with constant shaking at 40°C for 1 h. The ^{64}Cu-αCD11b was purified by a PD-10 column with ×1 phosphate-buffered saline, and eluent (3.0–4.5 mL) was collected. The number of DOTA per αCD11b antibody was calculated as moles (Cu^{2+}) × activity (3.0–4.5 mL)/moles (DOTA-αCD11b)/total activity (loaded for each labeling). The activities in the equation were all decay-corrected to the same time point. The results were expressed as mean ± SD (n = 3).

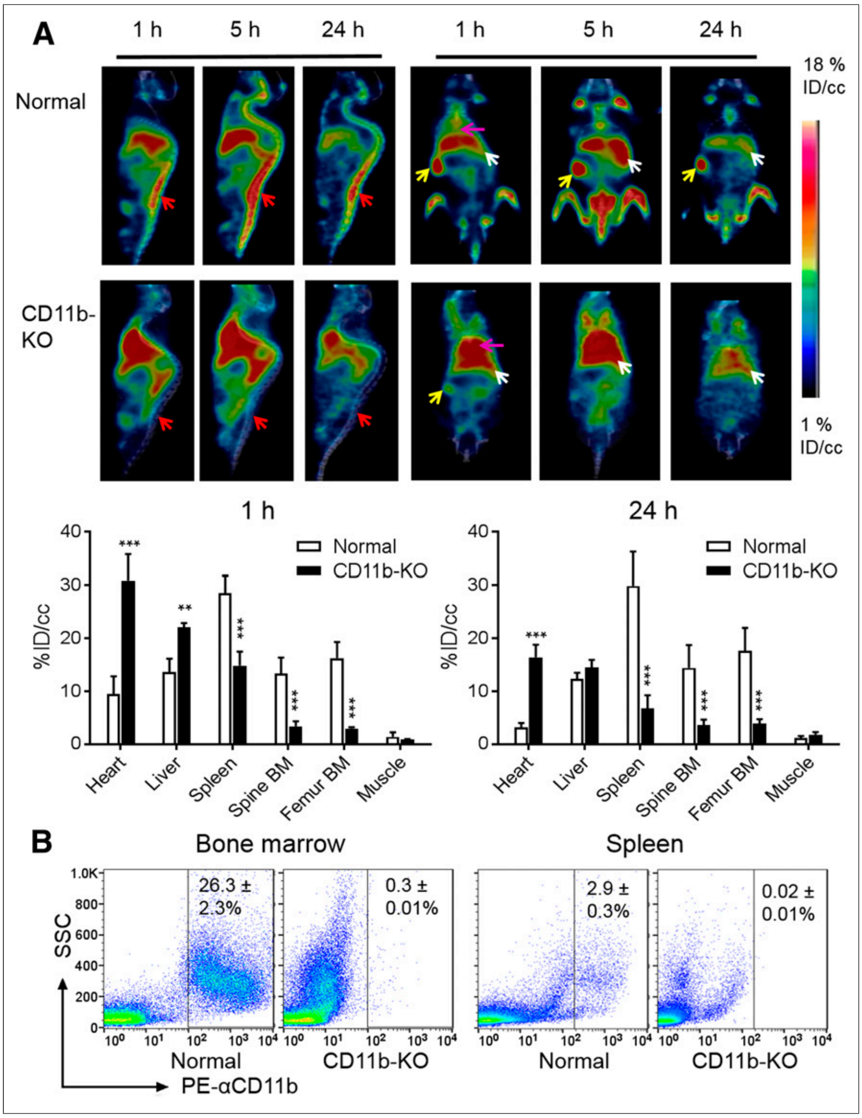

FIGURE 1. ^{64}Cu-αCD11b PET/CT in control (CD11b-sufficient) and CD11b-knockout C57BL/6 mice. (A) Representative PET/CT images of control mice (top) and CD11b-knockout (KO) mice (bottom). Red arrows: BM; yellow arrows: spleen; white arrows: liver; purple arrows: heart. PET quantification of ^{64}Cu-αCD11b uptake is shown in major organs at 1 h and 24 h after intravenous injection of radiotracer. (B) Flow cytometry analysis of CD11b$^+$ cells in BM and spleen of control and CD11b knockout (CD11b-KO) mice. All data are expressed as mean ± SD (n = 3/group). **$P < 0.01$. ***$P < 0.001$.

Competitive Cell-Binding Assay

Freshly isolated BM cells from C57BL/6 mice were suspended in phosphate-buffered saline containing 0.5% bovine serum albumin (1×10^5 cells per 200 μL). Cells were incubated with ^{64}Cu-αCD11b (3.7 kBq/well, ~4 × 10^{-10} M) in the absence and presence of increasing concentrations of nonradioactive αCD11b at room temperature for 2 h with gentle shaking. After removal of culture medium under vacuum, cells were washed 3 times with phosphate-buffered saline containing 0.1% bovine serum albumin. Radioactivity of the cells from each well was counted with a γ-counter. The 50% inhibitory concentration of nonradioactive αCD11b was calculated by fitting the data with nonlinear regression using GraphPad Prism (GraphPad Software).

Animal Models

All animal experiments were performed in compliance with the guidelines for care and use of research animals established by the Institutional Animal Care and Use Committee of the University of Texas M.D. Anderson Cancer Center (IACUC protocol 00001333). Female BALB/c mice and C57BL/6 mice (6–8 wk of age) were obtained from Taconic. CD11b$^{-/-}$ (CD11b knockout) C57BL/6 mice (B6.129S4-Itgamtm1Myd/J, stock number 003991) were purchased from the Jackson Laboratory.

Ear Inflammation Model. Twenty microliters of TPA solution (100 μg/mL in acetone) were topically applied to the ventral and dorsal sides of the right ear of BALB/c mice 1, 4, or 11 times (*8,16*).

Lung Inflammation Model. BALB/c mice were anesthetized with 2% isoflurane, and then 20 μg of lipopolysaccharide in 0.1 mL of saline were given intratracheally. Control animals were given 0.1 mL of saline intratracheally (*17*).

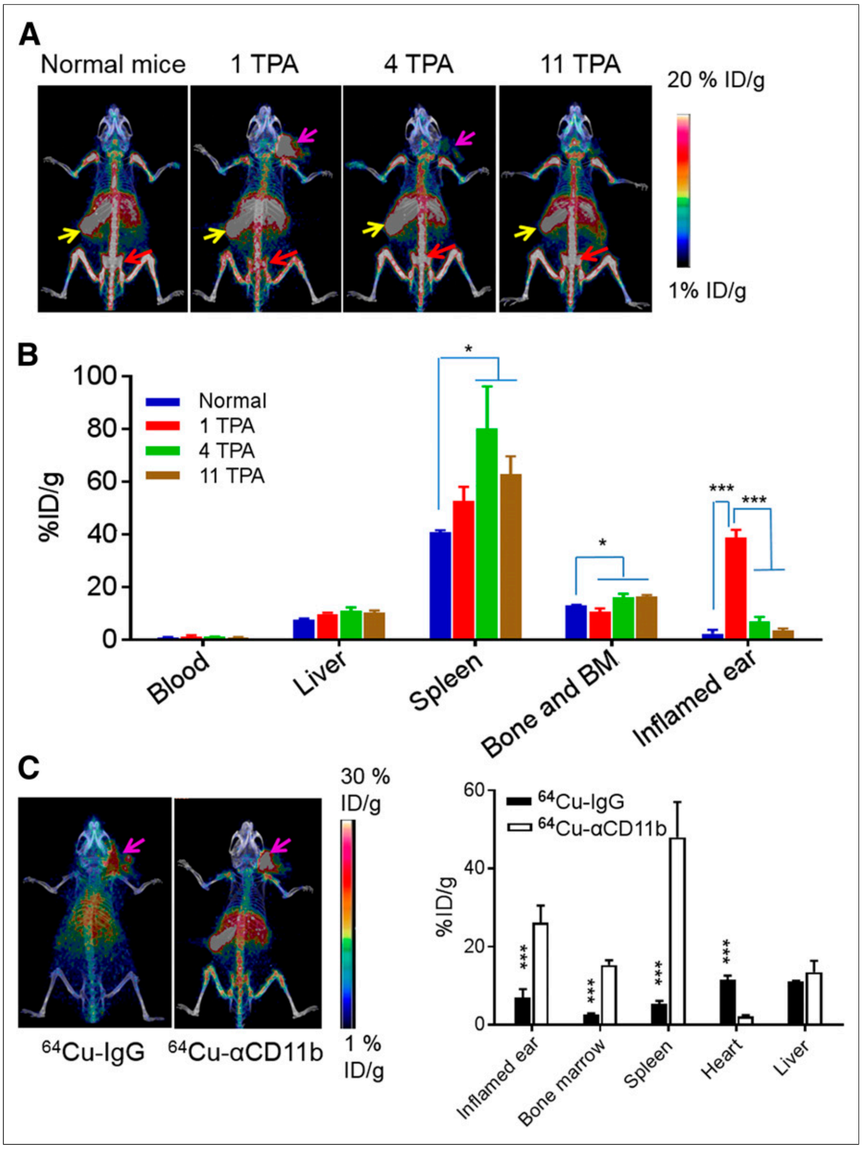

FIGURE 2. ^{64}Cu-αCD11b PET/CT and biodistribution of ^{64}Cu-αCD11b in BALB/c mice with TPA-induced acute and chronic ear inflammation. (A) Representative PET/CT images of control mouse, mouse with acute inflammatory focus after single TPA challenge in ear, and mice with chronic inflammatory foci after 4 and 11 TPA challenges. Images were acquired 24 h after intravenous injection of ^{64}Cu-αCD11b. Purple arrows: inflamed ears; red arrows: BM; yellow arrows: spleen. (B) Biodistribution of ^{64}Cu-αCD11b in control mice and mice with 1, 4, and 11 TPA challenges. Data were collected 48 h after intravenous injection of ^{64}Cu-αCD11b. (C) Representative PET/CT images and corresponding quantitative analysis comparing ^{64}Cu-IgG control antibody to ^{64}Cu-αCD11b in mice with acute ear inflammation after single TPA challenge. Data are expressed as mean ± SD (n = 3/group). *$P < 0.05$. ***$P < 0.001$.

PET/CT and Biodistribution

PET/CT was performed using an Inveon or Albira scanner after intravenous injection of ^{64}Cu-αCD11b or its corresponding isotype antibody control ^{64}Cu-IgG at a dose of 3.7 MBq/mouse (1.22 ± 0.22 μg antibody/3.7 MBq/mouse). The mice were euthanized 24 or 48 h after injection. Blood, major organs, and inflamed tissue specimens were collected, wet-weighed, and counted with a γ-counter (Packard). The results were reported as mean %ID/g and SD (n = 3/group).

PET Imaging Quantification

For each PET scan, 3-dimensional regions of interest were drawn over the major organs or inflammatory lesions on decay-corrected whole-body coronal images. The average radioactivity concentration (accumulation) within an organ or inflammatory lesion was obtained from mean pixel values within the region-of-interest volume and then converted to percentage injected dose per gram of tissue (%ID/g) or percentage injected dose per cubic centimeter of tissue (%ID/cc). Imaging data acquired from the Inveon scanner (Siemens) were analyzed using Inveon software (Siemens) and expressed as %ID/g. Imaging data acquired from the Albira scanner (Bruker) were analyzed using PMOD software (PMOD Technologies, Ltd.) and expressed as %ID/cc.

Autoradiography

Immediately after the PET/CT imaging, the ears were harvested and then taped to a chilled autoradiography cassette containing a Super Resolution screen (Packard) and stored overnight at 4°C. Screens were scanned with a Fujifilm FLA-5100 imaging system.

Hematoxylin–Eosin and Immunohistochemistry Staining

For hematoxylin–eosin staining, organ samples were fixed in 10% (v/v) buffered formalin and embedded in paraffin. Five-micrometer-thick sections were cut and stained with hematoxylin–eosin. For immunohistochemistry staining, the formalin-fixed paraffin sections were deparaffinized, rehydrated, and incubated in 3% aqueous H_2O_2 to block the endogenous peroxidase activity. After blocking with 2% normal horse serum, the primary antibody rat antimouse Ly6G (eBioscience Inc.) at 1:50 dilution was added and incubated at 4°C overnight. Immunohistochemistry reaction was performed using Vectastain Elite ABC HRP kit (rat IgG) (Vector Laboratories).

Flow Cytometry

BM cells were obtained from mouse femur according to reported procedures (*18*). For flow cytometry, fluorescence probes were added to single-cell suspensions prepared from samples obtained from BM or spleen, and cells were incubated on ice for 1 h. After washing with phosphate-buffered saline 3 times, cells were examined on a FACSCalibur flow cytometer or LSRFortessa X-20 analyzer (Becton Dickinson) and analyzed with FlowJo software (Tree Star, Inc.). The following antibodies were used: rat antimouse Ly6G-FITC, rat antimouse CD11b-phycoerythrin, rat antimouse Gr-1-PerCP-cyanine5.5, and antimouse Ly6C-allophycocyanin.

Statistics

Statistical significance was analyzed with IBM SPSS statistics 24 software using 1-way ANOVA. P values of less than 0.05 were considered statistically significant.

RESULTS

^{64}Cu-αCD11b Selectively Binds to CD11b^{+} Myeloid Cells

The binding affinity between ^{64}Cu-αCD11b and mouse BM cells was determined by a competitive displacement assay. The

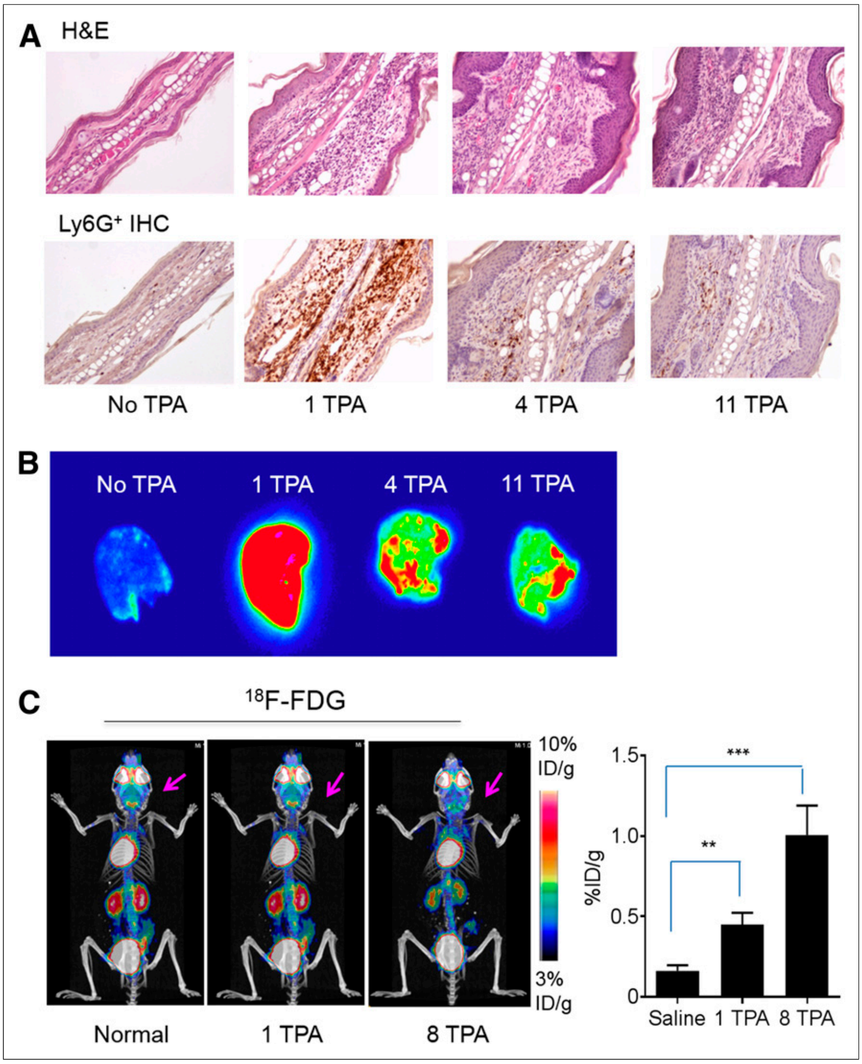

FIGURE 3. Histologic and immunohistochemistry confirmation of local inflammatory response in TPA-treated ears. (A) Representative images of sections of hematoxylin- and eosin-stained (H&E) and immunohistochemistry-stained (IHC) inflamed ears (×200). (B) Autoradiographs of ears from mice with different TPA treatments removed 48 h after intravenous injection of ^{64}Cu-αCD11b. (C) Representative ^{18}F-FDG PET/CT image of control mouse and mice with 1 and 8 TPA challenges in ears. Arrows: inflamed ears. corresponding quantitative analysis of ^{18}F-FDG uptake in ears are shown. Data are expressed as mean ± SD (n = 3/group). $^{**}P < 0.01$. $^{***}P < 0.001$.

50% inhibitory concentration between ^{64}Cu-αCD11b and nonradioactive αCD11b was $1.56 \times 10^{-10} \pm 5.14 \times 10^{-11}$ mol/L (Supplemental Fig. 1).

Figure 1A compares PET/CT images acquired at various times after intravenous injection of ^{64}Cu-αCD11b in control (normal mice) (i.e., CD11b-sufficient) and CD11b knockout (CD11b$^{-/-}$) C57BL/6 mice. In control mice, the radiotracer was distributed primarily to the BM, spleen, and liver. Strong signals from the spinal cord, hip bones, and joints could be visualized as early as 1 h after injection and peaked at 5 h after injection, suggesting robust uptake of ^{64}Cu-αCD11b to the BM (which bears CD11b$^+$ cells). The high uptake of ^{64}Cu-αCD11b in the spleen is consistent with the fact that the mouse spleen harbors half the body's monocytes within its red pulp (*19*). In contrast, in the CD11b knockout mice, the amount of ^{64}Cu-αCD11b in the blood pool (heart) was significantly higher than that in control mice at all time points studied ($P < 0.001$). However, the uptake of ^{64}Cu-αCD11b in the BM and spleen was significantly lower in the CD11b knockout mice than in the wild-type mice (Fig. 1A; Supplemental Figs. 2 and 3). Uptake of ^{64}Cu-αCD11b in the liver was also greater in knockout mice, likely in part because of increased blood-pool activity. The observation that uptake in the heart and liver is nonspecific is also supported by the use of nonspecific IgG, as discussed below.

Flow cytometry analysis performed 48 h after radiotracer injection confirmed that the percentage of CD11b$^+$ cells in the BM was 26.3% ± 3.0% in control mice versus 0.27% ± 0.01% in CD11b$^{-/-}$ mice (Fig. 1B; Supplemental Fig. 4). Likewise, the percentage of CD11b$^+$ cells in the spleen was 2.9% ± 0.3% in control mice versus 0.02% ± 0.01% in CD11b$^{-/-}$ mice (Fig. 1B). These data indicate that ^{64}Cu-αCD11b specifically bound to CD11b$^+$ myeloid cells in vivo.

After peaking at 5 h, the uptake of ^{64}Cu-αCD11b in the BM of control mice steadily and significantly decreased from 5 h to 24 h and 48 h after injection ($P < 0.001$), whereas uptake of ^{64}Cu-αCD11b in the BM of knockout mice remained low at background levels, unchanged from 24 to 48 h (Supplemental Figs. 3C and 3D). This finding might be attributed to redistribution of ^{64}Cu-αCD11b–bound myeloid cells from the BM to the peripheral circulation in control mice, clearance of radiotracer, or both.

In control BALB/C mice, ^{64}Cu-αCD11b displayed a distribution pattern similar to that in control C57BL/6 mice: BM, spleen, and liver were the organs with major radiotracer uptake (Supplemental Figs. 5A and 5B). CD11b$^+$ cells were the major cell population in the BM of BALB/c mice: 37.5% ± 1.92% of the BM cells expressed CD11b (Supplemental Fig. 5C).

^{64}Cu-αCD11b PET Differentiates Different Stages of TPA-Induced Local Inflammation

We first investigated changes in the distribution pattern of CD11b$^+$ myeloid cells at the local level in response to TPA-induced inflammation in the ears of BALB/c mice. PET/CT images acquired 24 h after intravenous injection of ^{64}Cu-αCD11b showed significantly higher uptake in the inflamed ears 30 h after a single TPA challenge, during the acute inflammation stage (Fig. 2A). In comparison, when 4 or 11 TPA challenges were administered and imaging was done 8 or 22 d after the first challenge during the chronic inflammation stage, significantly less CD11b$^+$ signal was seen within the inflamed ear. There was minimal radiotracer uptake in the contralateral, unchallenged ears or ears of control mice (Fig. 2A). These PET/CT data were confirmed by a classic biodistribution study (Fig. 2B).

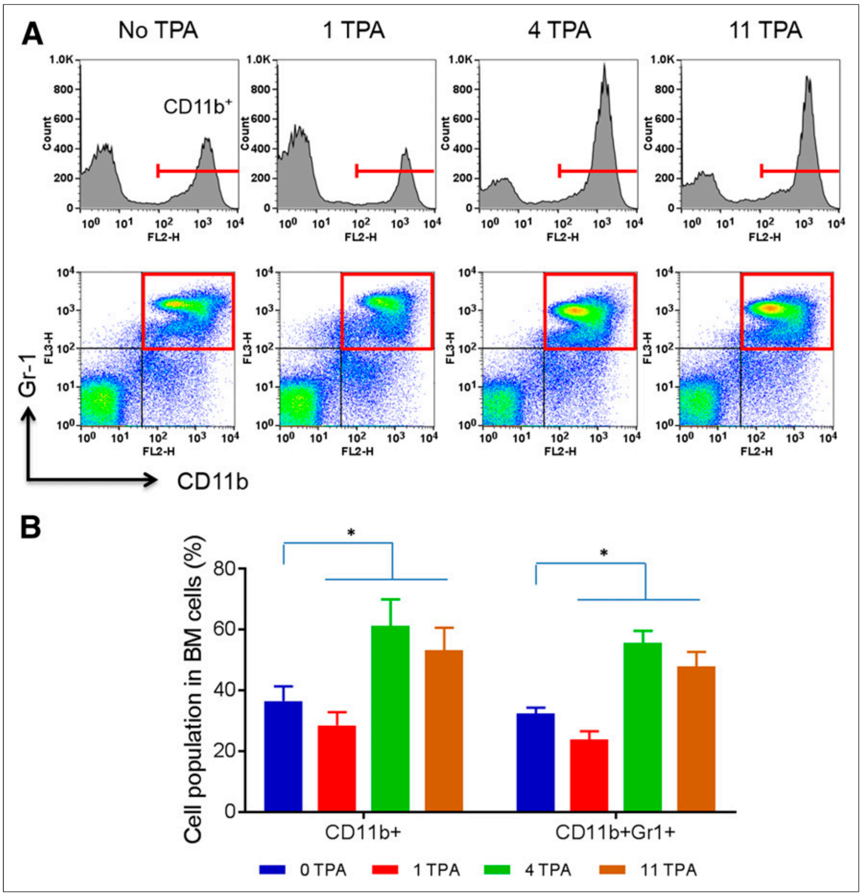

FIGURE 4. Flow cytometry analysis of BM cells from mice with TPA-induced ear inflammation. (A) $CD11b^+$ cells and $CD11b^+Gr\text{-}1^+$ double-positive cells from BM in mice with inflamed ears after 1, 4, and 11 TPA challenges. (B) Flow cytometric quantitation of percentages of $CD11b^+$ cells and $CD11b^+Gr\text{-}1^+$ cells in whole BM cells in control mice (0 TPA) and mice with 1, 4, and 11 TPA challenges. All data are expressed as mean ± SD ($n = 3$/group). $^*P < 0.05$.

To exclude the possibility of nonspecific uptake of antibody in acute inflammation, we used ^{64}Cu-IgG as a control. PET/CT showed low deposition of ^{64}Cu-IgG in the BM and spleen (Fig. 2C), with most of the signal being detected in the heart and liver, a distribution pattern typical of nonspecific antibodies (*20*). Quantitative analysis showed that ^{64}Cu-αCD11b uptake in the ears with acute inflammation was 3.8 times that of ^{64}Cu-IgG ($P < 0.001$), further supporting that ^{64}Cu-αCD11b selectively bound to $CD11b^+$ myeloid cells in acute inflammatory lesions in vivo. Immunohistochemistry staining of Ly6G, a marker for myeloid-derived granulocytes and neutrophils ($CD11b^+Ly6G^+$) (*21*), showed infiltration of the inflamed ears by a large number of $Ly6G^+$ neutrophils 30 h after a single TPA challenge (Fig. 3A). Neutrophils are among the first inflammatory cells to migrate toward a site of inflammation. In contrast, multiple applications of TPA produced a chronic inflammatory reaction characterized by increased ear thickness (Supplemental Fig. 6) and diminished $Ly6G^+$ neutrophils (Fig. 3A).

Autoradiography 48 h after intravenous injection of ^{64}Cu-αCD11b showed minimal radioactivity in normal ears (Fig. 3B), and intense radioactivity in ears after a single TPA challenge, consistent with extensive neutrophil infiltration, but decreased radioactivity in ears with 4 or 11 TPA challenges, consistent with decreased neutrophil infiltration in ears with chronic inflammation.

PET with ^{18}F-FDG, which tracks elevated glucose metabolism, is a clinically established technique to assess the metabolic activity of inflammatory processes. In both acute and chronic inflammation in BALB/c mice, the inflamed ears were barely visible with ^{18}F-FDG PET/CT (Fig. 3C; Supplemental Fig. 7). Nevertheless, the uptake of ^{18}F-FDG in the ears after a single TPA challenge and after 8 TPA challenges was significantly higher than the uptake in normal ears, indicating low but increased metabolic activity in the inflamed ears. On comparison, the uptake of ^{18}F-FDG in the inflamed ears (0.45–1.00 %ID/g) was much lower than the uptake of ^{64}Cu-αCD11b in the ears with either acute inflammation (38.7 %ID/g) or chronic inflammation (3.6–6.9 %ID/g). Taken together, these data indicate that ^{64}Cu-αCD11b PET/CT is more effective in differentiating acute from chronic inflammation than is tracking changes in metabolic activity with ^{18}F-FDG PET/CT.

PET with ^{64}Cu-αCD11b Detects TPA-Induced Inflammation at Systemic Level

In mice with ear inflammation, ^{64}Cu-αCD11b PET/CT revealed a small decrease in the uptake of ^{64}Cu-αCD11b in the BM after a single TPA challenge. Interestingly, BM uptake of ^{64}Cu-αCD11b was significantly higher after 4 and 11 TPA challenges than after a single TPA injection (Fig. 2A). ^{64}Cu-αCD11b uptake in the spleen increased after a single TPA challenge and further increased after additional TPA challenges (Fig. 2A; Supplemental Fig. 8). Uptake of radiotracer in the bone (including BM) of control mice and mice with 1, 4, and 11 TPA challenges was 13.1 ± 0.25, 10.6 ± 1.34, 15.9 ± 1.55, and 16.3 ± 0.69 %ID/g ($P < 0.05$ for all comparisons with control mice), respectively (Fig. 2B). These data likely underestimated the uptake values in the BM because the weight of the cortical bone was included in the calculation of ID%/g values. Thus, changes in $CD11b^+$ myeloid cells in the BM and spleen could be readily visualized using ^{64}Cu-αCD11b PET/CT.

Flow cytometry analysis showed that $CD11b^+$ cells in the BM cells of control mice and mice with 1, 4, and 11 TPA challenges were 36.5% ± 4.8%, 28.5% ± 4.4%, 61.2% ± 8.8%, and 53.2% ± 7.5%, respectively (Figs. 4A and 4B). Furthermore, the $CD11b^+Gr\text{-}1^+$ double-positive cells, consisting of myeloid progenitors and immature granulocytes, macrophages, and dendritic cells, in the BM cells of control mice and mice with 1, 4, and 11 TPA challenges were 32.3% ± 2.0%, 23.9% ± 2.7%, 55.5% ± 4.1%, and 47.9% ± 4.7%, respectively (Figs. 4A and 4B). These findings were consistent with the ^{64}Cu-αCD11b PET/CT data that revealed an initial depletion of $CD11b^+$ cells in acute inflammation followed by an expansion of $CD11b^+$ cells in chronic inflammation in the BM (Fig. 2A).

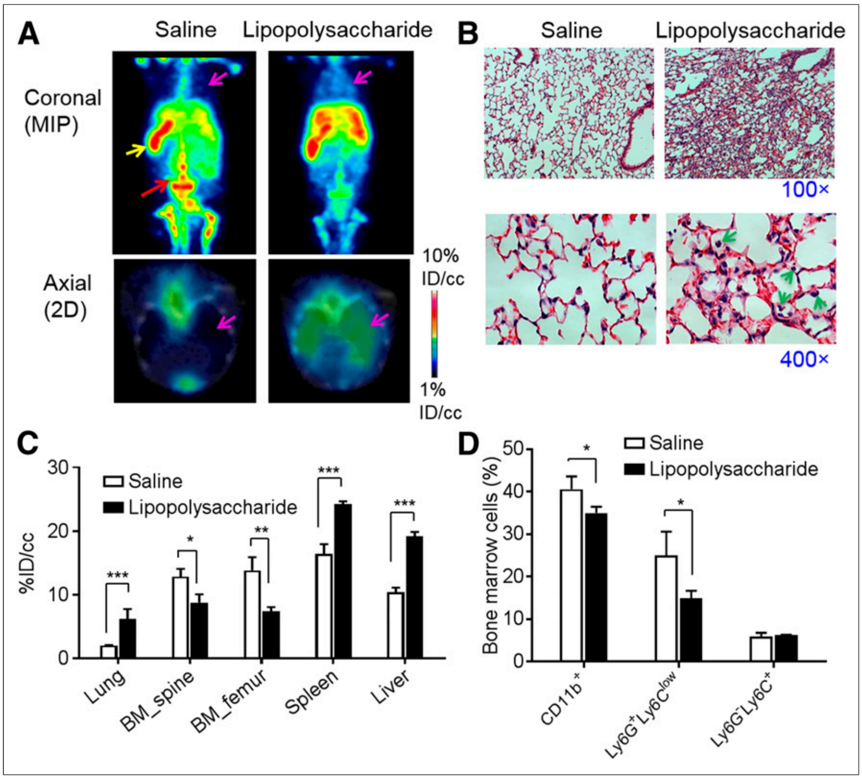

FIGURE 5. PET/CT of ^{64}Cu-αCD11b in BALB/c mice with lipopolysaccharide-induced acute lung inflammation. (A) Representative PET/CT images of control mouse with intratracheal instillation of saline and mouse with acute inflammation in lung induced by intratracheal instillation of lipopolysaccharide. Images were acquired 24 h after intravenous injection of ^{64}Cu-αCD11b and 28 h after lipopolysaccharide instillation. Purple arrows: inflamed lung; red arrow: BM; yellow arrow: spleen. MIP = maximum intensity projections; 2D = 2-dimensional. (B) Representative hematoxylin- and eosin-stained lung tissues. Green arrows: granular leukocytes. (C) PET imaging quantification of ^{64}Cu-αCD11b in control mice and mice with lung inflammation at 24 h. (D) Flow cytometry analysis of BM cells from control mice and mice with acute lung inflammation performed at 24 h. Data are expressed as mean ± SD (n = 3/group). $^{*}P < 0.05$. $^{**}P < 0.01$. $^{***}P < 0.001$.

PET with ^{64}Cu-αCD11b Detects Endotoxin-Induced Lung Inflammation at Local and Systemic Levels

Lung inflammation induced by intratracheal lipopolysaccharide closely reflects human lung inflammation (*22*). PET/CT 24 h after intravenous injection of ^{64}Cu-αCD11b (28 h after intratracheal injection of lipopolysaccharide) revealed higher radiotracer accumulation in the lungs, spleen, and liver and lower radiotracer signal in the BM of mice with lipopolysaccharide treatment (Fig. 5A). The lipopolysaccharide-treated lungs showed an increased thickness of the alveolar walls and increased neutrophil infiltration (Fig. 5B). There was significantly higher uptake of ^{64}Cu-αCD11b in the lungs of lipopolysaccharide-treated mice (6.23 ± 1.57 %ID/cc) than in the lungs of control mice (2.03 ± 0.09 %ID/cc, $P < 0.01$) 24 h after radiotracer injection (Fig. 5C). Lipopolysaccharide-treated mice exhibited significantly lower radiotracer uptake in the spine (8.8 ± 1.2 %ID/cc vs 12.9 ± 1.2 %ID/cc, $P < 0.05$) and femoral BM (7.4 ± 0.7 %ID/cc vs 13.8 ± 2.1, $P < 0.01$) than did control mice. These lipopolysaccharide-treated mice also showed significantly higher radiotracer uptake in the spleen (24.3 ± 0.4 %ID/cc vs 16.4 ± 1.5 %ID/cc; $P < 0.001$), as well as the liver (19.2 ± 0.7 %ID/cc vs 10.4 ± 0.7 %ID/cc; $P < 0.001$). These CD11b^{+} cellular distribution patterns were similar to those observed in mice with TPA-induced acute ear inflammation.

Flow cytometry data revealed that the population of CD11b^{+} cells in the BM of lipopolysaccharide-treated mice decreased significantly compared with that of the control mice (Fig. 5D; Supplemental Fig. 9A), consistent with the ^{64}Cu-αCD11b PET imaging data. CD11b^{+}Gr-1^{+} cells consist of 2 major subsets: Ly6G^{+}Ly6C^{low} granulocytic cells and Ly6G^{-}Ly6C^{+} monocytic cells. Results showed a significant decrease in Ly6G^{+}Ly6C^{low} granulocytic cells but not Ly6G^{-}Ly6C^{+} monocytic cells in the BM of lipopolysaccharide-treated mice compared with values in control mice (Fig. 5D; Supplemental Fig. 9B). These results also demonstrated that ^{64}Cu-αCD11b PET/CT permitted visualization of the dynamic innate immune response at both the local inflammation site and at the whole-body level, after a localized immune challenge.

DISCUSSION

In this study, we found that ^{64}Cu-αCD11b specifically and robustly labeled CD11b^{+} myeloid cells in vitro and in vivo. ^{64}Cu-αCD11b PET/CT could track and quantify changes in the number of CD11b^{+} cells both at the local level at the inflammatory sites and at the systemic level in the BM and the secondary lymphoid organ (spleen).

Several lines of evidence suggest that ^{64}Cu-αCD11b specifically bound to CD11b^{+} cells in vivo. First, whereas the CD11b-sufficient C57BL/6 mice exhibited high radiotracer uptake in the BM and spleen, which are reservoir organs for CD11b^{+} cells, the CD11b-knockout mice had significantly lower uptake of the radiotracer in these organs and a significantly higher amount of ^{64}Cu-αCD11b in the blood pool (particularly the heart). Second, deposition of nonspecific ^{64}Cu-IgG in the BM and spleen of ear inflammation mice was significantly lower than the deposition of ^{64}Cu-αCD11b in these organs.

Our study showed that ^{64}Cu-αCD11b PET/CT could be used to differentiate acute from chronic local inflammation. ^{64}Cu-αCD11b PET/CT clearly delineated inflamed ears in the acute inflammation phase and reduced radiotracer uptake in the chronic inflammation phase. Immunohistochemistry staining confirmed the presence of a large number of neutrophil granulocytes (CD11b^{+}Ly6G^{+}) within the inflammatory lesions in the acute phase but only a small number of CD11b^{+}Ly6G^{+} granulocytes infiltrating the lesions in the chronic phase. It is known that during chronic inflammation, other types of immune cells responsible for tissue repair and remodeling, such as lymphocytes and fibroblasts that do not express CD11b, are the dominant inflammatory cells (*23*).

Importantly, our studies suggest that ^{64}Cu-αCD11b PET/CT may be used to noninvasively interrogate mobilization of innate immune cells from the BM through the spleen and liver compartments to the diseased sites. In mouse inflammation models, ^{64}Cu-αCD11b PET/CT demonstrated a decrease in BM radiotracer uptake in the acute inflammation phase and a significant increase in BM radiotracer uptake in the chronic inflammation phases. These imaging data were consistent with reduced CD11b^{+} and CD11b^{+}Ly6G^{+} cells in the BM in the acute inflammation phase and increased CD11b^{+} and CD11b^{+}Ly6G^{+} cells in the BM during chronic inflammation. Myeloid cells, in particular neutrophils, provide an important early defense mechanism against acute infection and inflammation. Under normal circumstances, most of the neutrophil pool is stored in the BM; only a small fraction of neutrophils enters the blood circulation at any given time (<2% of 65 million in the mouse) (*24*). Thus, the immediate need for a large number of neutrophils in the case of acute inflammation cannot be met by circulating neutrophils in the blood pool, leading to rapid mobilization of neutrophils from the BM. This dynamic but transient process of recruiting CD11b^{+} myeloid cells and CD11b^{+}Ly6G^{+} granulocytes from the BM and their trapping in the spleen and liver were readily detected and quantified using ^{64}Cu-αCD11b PET/CT. In the chronic inflammation phase, the system may be signaled to produce more myeloid cells, though this possibility needs verification using BrdU labeling studies. Likewise, extramedullary myelopoietic activity in the spleen may have contributed to the increased uptake of ^{64}Cu-αCD11b in the spleen, though this hypothesis needs further verification. To sum, ^{64}Cu-αCD11b PET/CT represents a powerful tool for studying the dynamics of the innate immune response locally and systemically in living animals.

Our finding that CD11b^{+} myeloid cells in the BM were readily accessible to ^{64}Cu-αCD11b contrasts with the findings reported by Rashidian et al. (*25*), who used a much smaller variable domain of a camelid heavy-chain–only antibody targeting CD11b (~15 kDa), ^{18}F-VHHDC13. Although this ^{18}F-labeled probe showed uptake in spleen and lymph nodes, there was no uptake in the BM. It may be that the αCD11b used in our study and VHHDC13 bind to different CD11b epitopes, which may be differentially expressed in BM-derived myeloid cells and in tumor-associated myeloid cells. It is also possible that the much larger αCD11b (~150 kDa) has a longer blood half-life than that of VHHDC13 (~20 min) and thus a greater likelihood of delivery to the cells in the BM.

Our study has a few limitations. First, CD11b is expressed on several different types of myeloid cells and on a few nonmyeloid cells as well. Additional imaging markers are needed to enhance cellular resolution. Second, the systemwide myeloid cell trafficking studies need to be expanded with accurate enumeration of CD11b cell numbers in various primary and secondary immune compartments, fortified with BrdU labeling studies. Third, whereas we have established that ^{64}Cu-αCD11b could image CD11b in murine models of disease, the clinical significance of this approach in comparison to other imaging methods currently used to assess inflammation remains to be determined.

CONCLUSION

PET/CT imaging with ^{64}Cu-αCD11b has the potential for tracking and quantifying changes in CD11b^{+} cell numbers longitudinally and noninvasively both locally and systemically.

DISCLOSURE

This work was supported by the John S. Dunn Foundation and by National Institutes of Health/National Cancer Institute Cancer Center Support Grant P30CA016672. No other potential conflict of interest relevant to this article was reported.

ACKNOWLEDGMENTS

We thank Stephanie Deming for editing this article and Daniel Young for help with preparing samples for histologic examinations. We thank the Flow Cytometry and Cellular Imaging Core Facility and Small Animal Imaging Facility at M.D. Anderson Cancer Center for their support.

KEY POINTS

QUESTION: Can we use PET/CT for longitudinal assessment of local and systemic immune response involving mobilization of CD11b^{+} myeloid cells?

PERTINENT FINDINGS: PET/CT with ^{64}Cu-labeled anti-CD11b antibody (^{64}Cu-αCD11b) successfully tracked and differentiated acute and chronic inflammation at local and systemic levels. ^{64}Cu-αCD11b small-animal PET/CT is a robust quantitative method for imaging systemic immune responses.

IMPLICATIONS FOR PATIENT CARE: ^{64}Cu-αCD11b PET/CT may be useful for noninvasive assessment of a number of diseases involving abnormal activity of CD11b+ myeloid cells, including infectious disease, autoimmune disease, and toxicity and responses to antitumor therapies.

REFERENCES

1. Hildebrandt IJ, Gambhir SS. Molecular imaging applications for immunology. *Clin Immunol.* 2004;111:210–224.
2. Gross S, Moss BL, Piwnica-Worms D. Veni, vidi, vici: in vivo molecular imaging of immune response. *Immunity.* 2007;27:533–538.
3. Germain RN, Miller MJ, Dustin ML, Nussenzweig MC. Dynamic imaging of the immune system: progress, pitfalls and promise. *Nat Rev Immunol.* 2006;6:497–507.
4. Laitinen IE, Luoto P, Nagren K, et al. Uptake of ^{11}C-choline in mouse atherosclerotic plaques. *J Nucl Med.* 2010;51:798–802.
5. Rudd JH, Myers KS, Bansilal S, et al. Atherosclerosis inflammation imaging with ^{18}F-FDG PET: carotid, iliac, and femoral uptake reproducibility, quantification methods, and recommendations. *J Nucl Med.* 2008;49:871–878.
6. Glaudemans AW, de Vries EF, Galli F, Dierckx RA, Slart RH, Signore A. The use of ^{18}F-FDG-PET/CT for diagnosis and treatment monitoring of inflammatory and infectious diseases. *Clin Dev Immunol.* 2013;2013:623036.
7. Peters AM, Saverymuttu SH, Reavy HJ, Danpure HJ, Osman S, Lavender JP. Imaging of inflammation with indium-111 tropolonate labeled leukocytes. *J Nucl Med.* 1983;24:39–44.
8. Cao Q, Cai W, Li ZB, et al. PET imaging of acute and chronic inflammation in living mice. *Eur J Nucl Med Mol Imaging.* 2007;34:1832–1842.
9. Palestro CJ. Radionuclide imaging of musculoskeletal infection: a review. *J Nucl Med.* 2016;57:1406–1412.
10. Hammoud DA. Molecular imaging of inflammation: current status. *J Nucl Med.* 2016;57:1161–1165.
11. Gordon S, Taylor PR. Monocyte and macrophage heterogeneity. *Nat Rev Immunol.* 2005;5:953–964.
12. Gabrilovich DI, Nagaraj S. Myeloid-derived suppressor cells as regulators of the immune system. *Nat Rev Immunol.* 2009;9:162–174.
13. Cai W, Wu Y, Chen K, Cao Q, Tice DA, Chen X. In vitro and in vivo characterization of ^{64}Cu-labeled Abegrin, a humanized monoclonal antibody against integrin alpha v beta 3. *Cancer Res.* 2006;66:9673–9681.
14. Meares CF, McCall MJ, Reardan DT, Goodwin DA, Diamanti CI, McTigue M. Conjugation of antibodies with bifunctional chelating agents: isothiocyanate and

bromoacetamide reagents, methods of analysis, and subsequent addition of metal ions. *Anal Biochem.* 1984;142:68–78.

15. Liu S, Li D, Park R, et al. PET imaging of colorectal and breast cancer by targeting EphB4 receptor with ^{64}Cu-labeled hAb47 and hAb131 antibodies. *J Nucl Med.* 2013;54:1094–1100.
16. Murakawa M, Yamaoka K, Tanaka Y, Fukuda Y. Involvement of tumor necrosis factor (TNF)-alpha in phorbol ester 12-O-tetradecanoylphorbol-13-acetate (TPA)-induced skin edema in mice. *Biochem Pharmacol.* 2006;71:1331–1336.
17. Li XC, Miyasaka M, Issekutz TB. Blood monocyte migration to acute lung inflammation involves both CD11/CD18 and very late activation antigen-4-dependent and independent pathways. *J Immunol.* 1998;161:6258–6264.
18. Weischenfeldt J, Porse B. Bone marrow-derived macrophages (BMM): isolation and applications. *CSH Protoc.* 2008;2008:pdb prot5080.
19. Swirski FK, Nahrendorf M, Etzrodt M, et al. Identification of splenic reservoir monocytes and their deployment to inflammatory sites. *Science.* 2009;325:612–616.
20. Wipke BT, Wang Z, Kim J, McCarthy TJ, Allen PM. Dynamic visualization of a joint-specific autoimmune response through positron emission tomography. *Nat Immunol.* 2002;3:366–372.
21. Kolaczkowska E, Kubes P. Neutrophil recruitment and function in health and inflammation. *Nat Rev Immunol.* 2013;13:159–175.
22. Rittirsch D, Flierl MA, Day DE, et al. Acute lung injury induced by lipopolysaccharide is independent of complement activation. *J Immunol.* 2008;180:7664–7672.
23. Aldaz CM, Conti CJ, Gimenez IB, Slaga TJ, Klein-Szanto AJ. Cutaneous changes during prolonged application of 12-O-tetradecanoylphorbol-13-acetate on mouse skin and residual effects after cessation of treatment. *Cancer Res.* 1985;45:2753–2759.
24. Raffaghello L, Bianchi G, Bertolotto M, et al. Human mesenchymal stem cells inhibit neutrophil apoptosis: a model for neutrophil preservation in the bone marrow niche. *Stem Cells.* 2008;26:151–162.
25. Rashidian M, Keliher EJ, Bilate AM, et al. Noninvasive imaging of immune responses. *Proc Natl Acad Sci USA.* 2015;112:6146–6151.